5
Symmetrical Dot Pattern Based Algorithm

This chapter focuses on the application of Symmetrical dot pattern for fault detection. A unique fault pattern for power system faults is proposed to distinguish between a healthy phase and a faulty phase. The potential of these unique patterns to eliminate the feature extraction process when used with Convolutional Neural Network is demonstrated with case studies.

Visually separable patterns are generated in mechanical systems for successful detection of faults. Symmetrical Dot (SDP) of faulty signals are utilized for visual fault diagnosis in literature. [Pickover, 1986] illustrated that in this method, the time varying data is visually represented in the form of a dot pattern. The variations in the amplitude and frequency can be depicted by transforming the time data after normalization onto a polar plot. [Shirai *et al.*, 1996] utilized these SDP variations for fault diagnosis of mechanical equipment. Normal and faulty fans are classified with the help of audio and vibration signals by [Shibata *et al.*, 2000] and [Xu *et al.*, 2016]. Fault identification in an internal combustion engine and diesel engine operating at different speeds is proposed by [Wu and Chuang, 2005] and [Zeng *et al.*, 2014] respectively. This technique, though has the potential to discriminate power system faults is not yet applied.

5.1 SYMMETRICAL DOT PATTERN

SDP is a signal processing method in which the time varying data sample in cartesian coordinate system $(t, S(t))$ is transformed into a new polar coordinate system having radial coordinate $A(t)$ and symmetrical angular coordinates $\psi(t)$ and $\phi(t)$. $\phi(t)$ is the angle of rotation in positive direction (counter clock wise) and $\psi(t)$ is the angle of rotation in negative direction (clock wise). Unlike normal polar coordinate system which has only one angular coordinate $\Theta(t)$, the SDP polar coordinate system has two angular coordinates to generate symmetry. The difference between the two polar coordinate systems is shown in Fig. 5.1.

The other major difference lies in the mapping of the data samples on the polar coordinate system. The normal polar coordinates at a time t_1, $(r(t_1), \Theta(t_1))$ correspond to the original data point $(t_1, S(t_1))$ itself. Whereas, in SDP, the radial coordinate $A(t_1)$ corresponds to the data sample

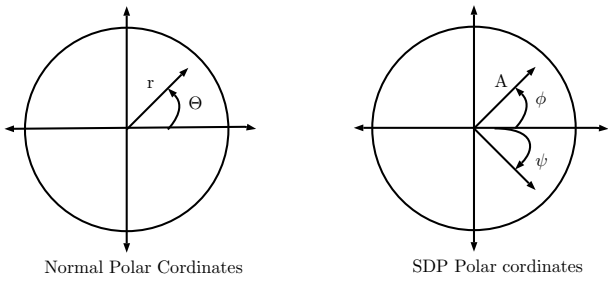

Figure 5.1: (a) Normal Polar Coordinate System (b) SDP Polar Coordinate System.

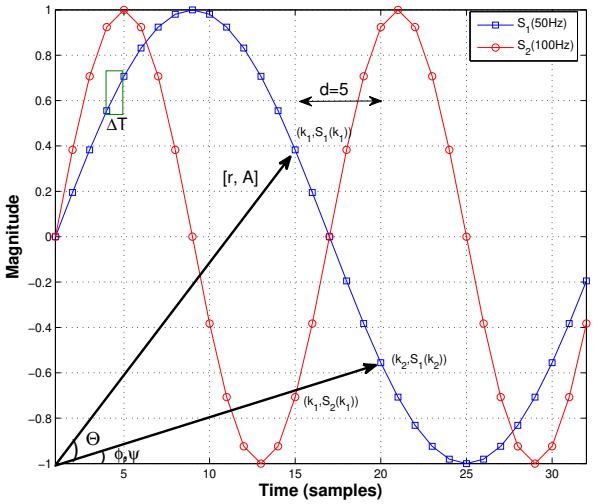

Figure 5.2: Sinusoidal signals with 50 Hz and 100 Hz frequency.

at time t_1 itself, which is $S(t_1)$, but the angular coordinates correspond to a data point with a certain sample delay d i.e, $S(t_1 + d.\Delta T)$. Here, ΔT is the sampling time of the data. The mapping of a data sample onto the new polar coordinate system is shown with the help of Fig. 5.2, in which two sinusoidal signals S_1 and S_2 are considered with frequencies of 50 Hz and 100 Hz respectively. For instance, a data sample $(k_1, S_1(k_1)$ corresponds to radial component A and the angular component for SDP is obtained from the data sample $(k_2, S_1(k_2))$ which is delayed by d samples (d=5). The time varying sampled data can be transformed to new polar coordinates to generate SDP using the equation (5.1) [Xu *et al.*, 2016]. By plotting the time varying signal onto this new polar coordinate system, a snowflake shaped graph is generated. The number of snow flakes is $2n$ for an n-fold symmetrical dot pattern.

$$
\begin{aligned}
A(t) &= \frac{S(t) - S_{\min}}{S_{\max} - S_{\min}} \\
\phi(t) &= \theta_s + \frac{S(t + d.\Delta T) - S_{\min}}{S_{\max} - S_{\min}}.K \\
\psi(t) &= \theta_s - \frac{S(t + d.\Delta T) - S_{\min}}{S_{\max} - S_{\min}}.K
\end{aligned}
\tag{5.1}
$$

where, θ_s is the angle of symmetry. If the angle of symmetry θ_s is chosen as 60^0, then a 6-fold symmetrical SDP ($\frac{360}{\theta_s}$) can be obtained along the angle of symmetry as shown in Fig. 5.3 for a sinusoidal signal.

The width of the snowflakes can be increased with the increase in the sample delay d. The overlapping of the snowflakes can be varied with the variation of gain K which is $\leq \theta_s$. The overlapping increases with the increase of K. The snow flakes also orient themselves towards the angle prescribed with this parameter, thus limiting the upper boundary of the snowflake. The effect of variations of d and K can be observed in Figs. 5.4(a) and (b) respectively. Further, the normalization of the data using maximum and minimum values (S_{max} and S_{min}) removes the difference in the strength of the signal.

Factors affecting the shape of the SDP

Though the shape of the snowflakes can be controlled using the parameters (θ_s, K, d) used in the equation (5.1) for better visualization of the image, the inherent properties of the signal also

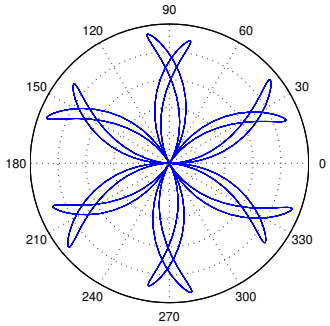

Figure 5.3: Six fold SDP for $\theta_s = 60^0$.

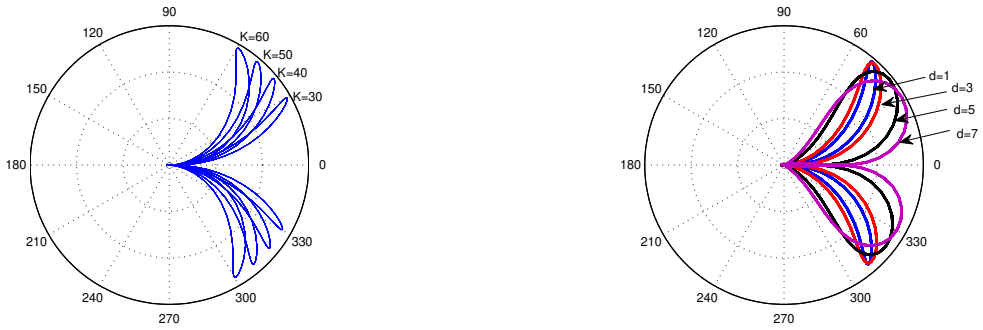

(a) (b)

Figure 5.4: SDP shape changes with parameters (a) Variation of $K = 30^0 - 60^0$ (b) Variation of $d = 1, 3, 5, 7$.

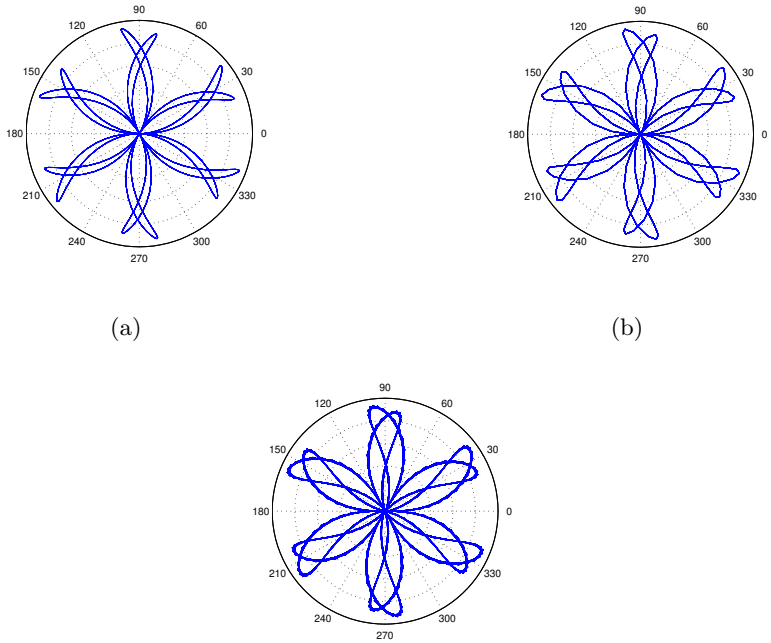

(a) (b)

(c)

Figure 5.5: SDP shape change with frequency (a) 60 Hz (b) 120 Hz (c) 180 Hz.

play a dominant role in the formation of an SDP. The frequency of the signal and the monotonic nature of the signal determine the shape of the SDP significantly as illustrated in the following subsections.

(a) Dependence on signal's frequency

With a change in the frequency of the signal, the angular coordinates and radial coordinates at any time instant k, may not remain constant. For example, the radial component at time instant $k_1 = 15$ for $S1(t)$ is 0.3827, whereas it is -0.507 for $S2(t)$ in Fig. 5.2. Also the angular coordinates are different as $S1(k_1 + d)$ is not equal to $S2(k_1 + d)$. Thus the SDP changes with system frequency. It is also observed that the SDP of sinusoidal signal with even harmonics has a smoother contour compared to the signal with odd harmonics. The width of the snowflake also increased enabling visual discrimination of odd harmonic content. A sinusoidal signal with three frequencies of 60 Hz (fundamental), 120 Hz (2nd harmonic) and 180 Hz (3rd harmonic) are considered to justify the statement with a sampling frequency of 1920 Hz in Figs. 5.5(a), (b) and (c) respectively.

(b) Dependence on signal's monotonic nature

A monotonically increasing function is one which never exhibits a decreasing trend. Similarly a monotonically decreasing function never shows an increasing trend. Mathematically, if a function $y = f(x)$ is continuous on [a, b] and it is differentiable on (a, b), then y is increasing if $\frac{dy}{dx} > 0$ for all $x \in (a, b)$. If the derivative $\frac{dy}{dx} < 0$ for all $x \in (a, b)$, then the function is decreasing. All the SDPs of the monotonically increasing or decreasing functions exhibit a unique pattern. As a case study three such functions are considered as shown in Fig. 5.6. All the functions have same number of data samples (32). The radial coordinate and the angular coordinate for these functions have a linear relationship. It is observed that only one sided snowflake is formed as the functions

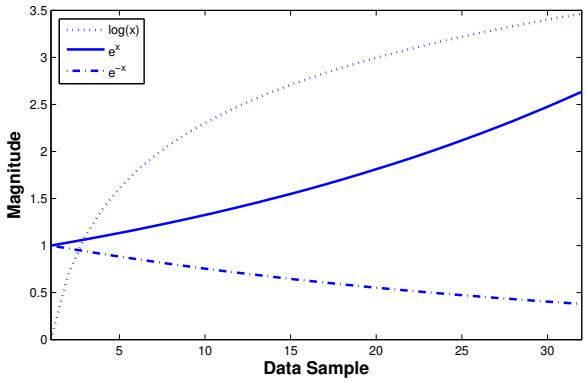

Figure 5.6: Monotonic Functions (a) log(x) (b) e^x (c) e^{-x}.

never return a zero value as shown in Fig. 5.7. The fault current also exhibit a monotonic trend depending on the fault inception angle. Since the EMD has the capability to extract the trend in the form of residue, the residue of the fault current also exhibit one sided snow flake which is established in this work.

5.2 CONVOLUTIONAL NEURAL NETWORK

Convolutional Neural Networks (CNNs) are widely used for classification problems using images. It is an emerging algorithm recently explored by power system researchers to solve fault diagnosis problems. It is successfully applied for fault detection in distribution network using wavelet contours generated from the zero sequence current signals by [Guo *et al.*, 2017]. [Tikariha *et al.*, 2021] proposed fault classification in IEEE 30 bus system using CNN directly without any pre-processing steps. The raw data of voltage and current signals are directly given as input without converting into an image. The raw data is sampled with a frequency of 2 kHz, and one cycle of post-fault information is fed to the CNN. However, the noise case and the effect of DG are not considered. In Rai *et al.* [2021], the faults are classified using CNN in the distribution network in the presence of DGs. A featureless approach is followed to obtain images from sampled raw current and voltage signals. However, a unique fault pattern is never proposed, which could be a potential feature for automatic fault detection with a combination of CNN to eliminate the feature extraction process. A brief introduction to CNN and various steps involved are presented here.

A Convolutional Neural Network is a deep learning algorithm similar to an artificial neural network that can take images as input to differentiate them into various classes. These networks transform input image data into complex features by processing the data in the form of arrays. It captures the spatio-temporal features in an image with the help of suitable filters [Manohar *et al.*, 2020]. There are various layers involved in this network.

Input Image This layer contains the grayscale image of the input data. Here the three phase current signals are transformed into gray scale images. An image is a matrix with the dimensions equivalent to that of pixels.

Convolutional layer In the convolution layer, the image is convolved with a 2D filter to obtain the feature vector. In other words, sampling of the image is carried out by sliding the filter of a size (mxn) over the entire image array. The same region of the input array can be processed with a number of filters corresponding to the number of connecting neurons. The feature vector is

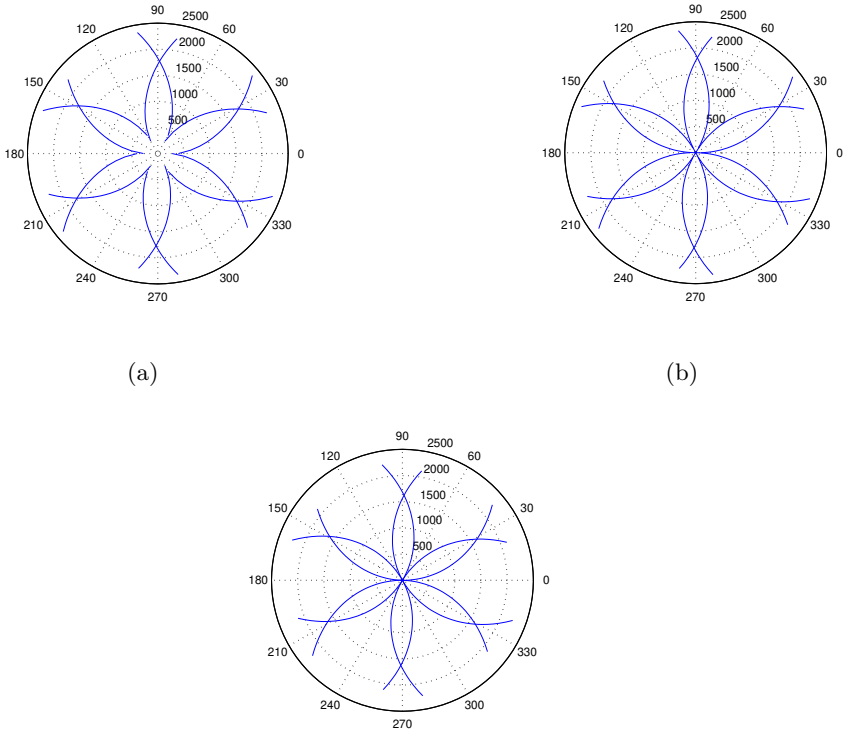

(a) (b)

(c)

Figure 5.7: SDP for monotonic functions (a) log(x) (b) e^x (c) e^{-x}.

obtained by the convolution of the input array ($g[x, y]$) and filter ($f[x, y]$) as

$$h(x, y) = f[x, y] * g[x, y] = \sum_{p=1}^{P} \sum_{q=1}^{Q} f[p, q].g[x - p, y - q] \tag{5.2}$$

where p, q represent the filter dimension and P, Q represent the dimension of input image.

ReLU Layer A nonlinear activation function, commonly known as rectified linear unit function, follows the convolution layer and performs mapping of $h(x, y)$. It is used to perform a threshold operation on each input received from the convolution layer and sets them as zero for any value less than zero. The ReLU layer does not alter the size of the image.

$$f(x, y) = \begin{cases} x & x > 0 \\ 0 & x \leq 0 \end{cases} \tag{5.3}$$

Pooling Layer In this layer the redundant information is removed by downsampling the feature space. This operation reduces the computational burden by reducing the dimension and also avoids overfitting. The layer extracts the maximum value from the specified rectangular size of the filter, which strides along the feature map obtained after the convolution and ReLU layers. The step size for striding is also specified.

Fully Connected Layer (FC Layer) This layer contains neurons that combine with all the neurons from the previous layers in order to identify larger patterns. The input to this layer is multiplied by a weight matrix and a bias. There can be more than one such layer, one followed by

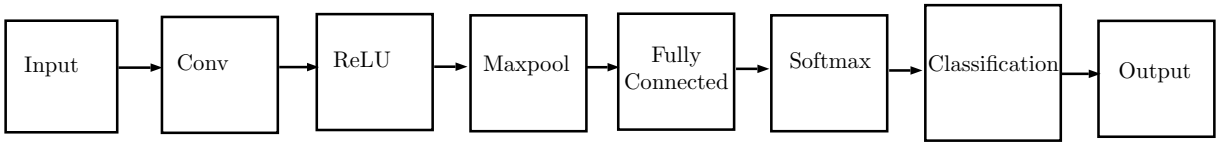

Figure 5.8: Various layers of CNN.

the other. However, the last layer should contain the neurons equal to the number of classes to be identified. In this work, the two classes of fault and healthy system are considered.

Softmax and classification layers For classification problems, these two layers immediately follow the last fully connected layer. A softmax function is applied to the input in the softmax layer. The output from the fully connected layer is normalized by the softmax layer and is also known as the normalized exponential. It converts numbers to probabilities. The classification layer immediately follows the softmax layer, where the cross-entropy loss for classification is computed and performs weighted classification tasks to classify various events. The output layer finally gives the classes. The various layers of the CNN are presented in Fig. 5.8.

5.3 TEST SYSTEM CONSIDERED

The proposed algorithm is tested on both the IEEE 13 bus and 34 bus systems using the same configurations as described in the Chapter 3 without any change. Also, the case studies used for fault are maintained the same.

5.4 PROPOSED ALGORITHM WITHOUT DG

Single Phase faults (AG, BG, CG), two phase faults (AB, BC, CA, ABG, BCG, CAG) and three phase faults (ABC, ABCG) are simulated at 0.5 s on an IEEE 13 bus system at all the bus locations with various fault incidence angles. The fault currents are extracted from substation (bus 650) and decomposed using EMD to obtain the residues R_a, R_b and R_c corresponding to each phase. An AG fault with zero fault incidence angle at bus 611 is shown in Fig. 5.9. The IMF and residue formed after EMD process inside the moving window containing half cycle post-fault data is shown in Fig. 5.10.

The residue formed from faulty phase could be either increasing or decreasing in nature depending on the fault incidence angle. Whereas the healthy phase after the fault would not yield any IMF thus making its residue equal to the signal itself. Now, SDP is generated for each phase utilizing their residues. The SDPs of three phases without fault being distinct are saved in a database and continuously correlated with the SDPs obtained at each new sample of the moving window. SNF_a is defined as the SDP of phase-A before fault (NF indicates No Fault) and SF_a is the SDP of phase-A after fault. The residue of a faulty phase being monotonic produces a unique SDP, thus making it is possible to generate visually separable feature. The type of fault can be classified with the number of unique patterns among the three phases. If the number of unique patterns is equal to N, then it is an N-Phase fault. In case of AG fault, N = 1, hence it correctly classifies it an LG fault. Though the faults can be detected and classified visually, a parameter is essential for a relay to take a decision. Therefore, a fault index (FI) is proposed based on the alienation coefficient of the patterns SF_a and SNF_a. The fault indices are then compared with a threshold to detect and classify the fault in a relay logic block. The block diagram of the proposed

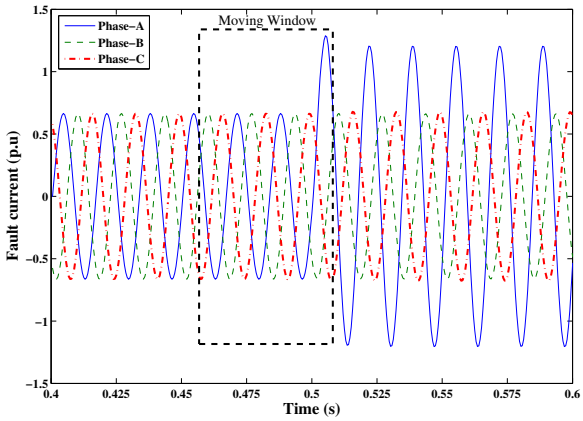

Figure 5.9: Fault currents at bus 650, AG fault at bus 611, FI= 0^0.

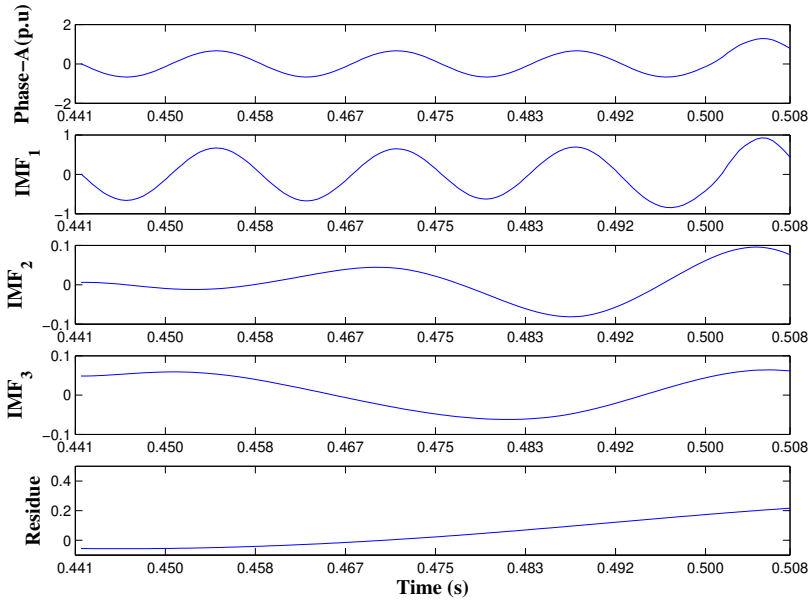

Figure 5.10: EMD decomposition of phase-A current.

algorithm is shown in Fig. 5.11.

5.4.1 Alienation of SDP Patterns

The correlation coefficient measures the similarity between two patterns. Correlation coefficient (r) of 2 two dimensional matrices M and N of size *pxq* is shown below,

$$r(M,N) = \frac{\sum_p \sum_q (M_{pq} - \bar{M})(N_{pq} - \bar{N})}{\sqrt{[\sum_p \sum_q (M_{pq} - \bar{M})^2][\sum_p \sum_q (N_{pq} - \bar{N})^2]}} \tag{5.4}$$

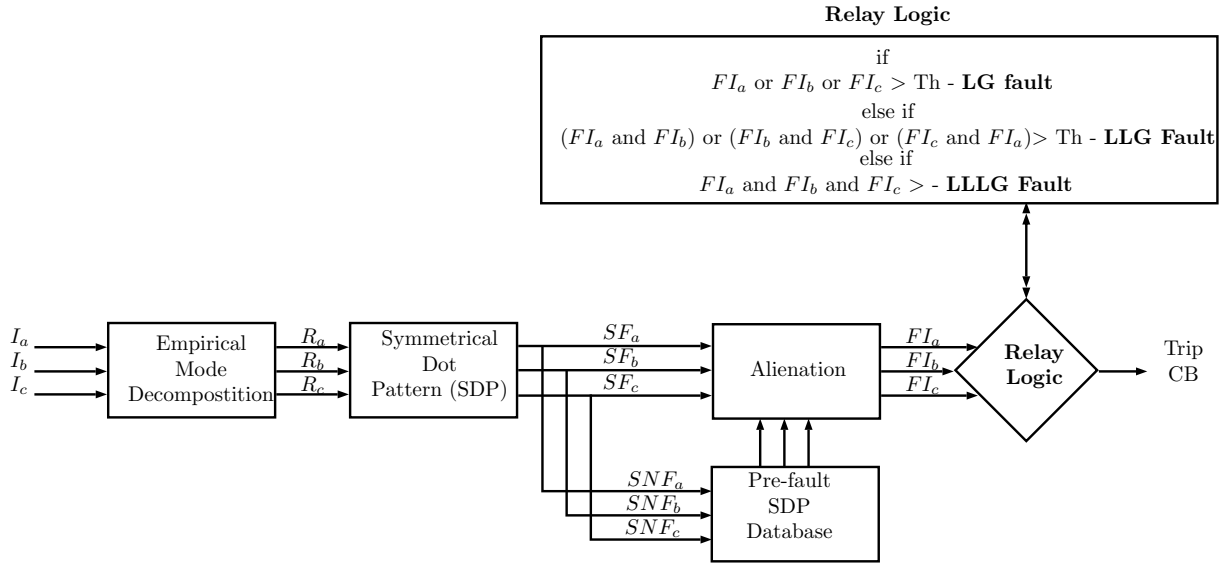

Figure 5.11: Block diagram of the proposed algorithm.

where, $\bar{M}$ and $\bar{N}$ are the mean of the matrices. The measure of uncorrelated patterns can be obtained by alienation coefficient

$$a(M,N) = 1 - r^2(M,N) \tag{5.5}$$

The SDP pattern obtained is converted into a two dimensional matrix of size *pxq* (gray scale image). The matrices corresponding to faulty and non faulty patterns must be of the same size. If the patterns are exactly same then $r = 1$ and $a = 0$ and if the patterns are completely different then the $r = 0$ and $a = 1$. Thus the value of fault index in the proposed algorithm can vary between 0 and 1.

5.4.2 Results and Discussion

The proposed algorithm is tested by considering various case studies involving changes in fault type, fault location, fault resistance, fault incidence angle. All the simulations are carried with a sampling frequency of 1.92 kHz. A moving window of 4 cycles is considered to generate the SDP patterns. The SDP parameters considered are (θ_s, K, d)=$(60^0, 40^0, 1)$ for all the cases. A threshold value of 0.4 is selected between minimum of FPI and maximum of HPI computed using 0.325 cycle post-fault data.

Variation of Moving window size

The size of the moving window determines the computational burden on the algorithm. Larger the size of the moving window greater is the computational burden. Thus the proposed algorithm is tested with variation in the size of moving window. Three such moving windows of sizes 6 cycles, 4 cycles and 2 cycles are considered to evaluate the SDP formation and thereby the fault detection capability. It is observed that the FPI is above the threshold and HPI is below the threshold in all the three cases as shown in Fig. 5.12. Also the difference between the FPI and HPI reduced by decreasing the moving window size. Therefore the moving window size is chosen as 4 cycles in this research work to avoid non detection of fault with further reduction of window size.

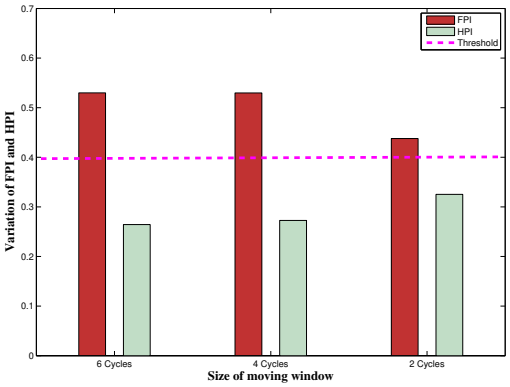

Figure 5.12: Variation of moving Window size.

Variation of type of fault

The fault transients are dependent on the type of the fault and the involvement of ground. The SDPs for various fault types at bus 611 are shown in Table 5.1. It is evident that the SDP of only the faulty phase is different from that of the healthy phase. The faulty phase exhibits one sided snow flake whereas the healthy phase exhibits two sided normal snow flake. Also the variation of fault index with time is shown in Fig. 5.13. It can be observed that only the faulty phases B, AC, AB and ABC are above the threshold as indicated in Figs. 5.13(a), (b), (c) and (d) respectively. Also the fault index variation is localized exactly at the fault time of 0.5 s.

Variation of fault location

The fault transients are also dependent on the location of the fault. Thus all the faults are simulated at every bus of the IEEE 13 bus system. The proposed algorithm successfully detects the fault occurring at various locations as shown in Fig. 5.14. The FPI is above the threshold at all locations and the HPI is below the threshold indicating that the proposed algorithm is immune to the variations in the location of the fault.

Variation of fault incidence angle

The proposed algorithm is verified for various fault incidence angles (FIA) of 0^0, 30^0, $60^0, 90^0, 120^0, 150^0$. It is observed that the proposed algorithm successfully detects the fault for all incidence angles considered. The fault index variations for ABCG, ABG, AB and AG faults at bus 632 are only shown. The fault index value of all faulty phases A, B and C are above the threshold for ABCG fault as shown in Fig. 5.15(a). In the case of ABG and AB faults only phase C is below the threshold indicating that the fault is present in phases A and B only as shown in Fig. 5.15(b) and Fig. 5.15(c) respectively. Also it can be noted that the phase-C fault index is zero for all fault incidence angles for AB fault whereas it is significant and classifies the involvement of ground in ABG type fault. Phases B and C have fault index value below the threshold for an AG fault as illustrated in Fig. 5.15(d).

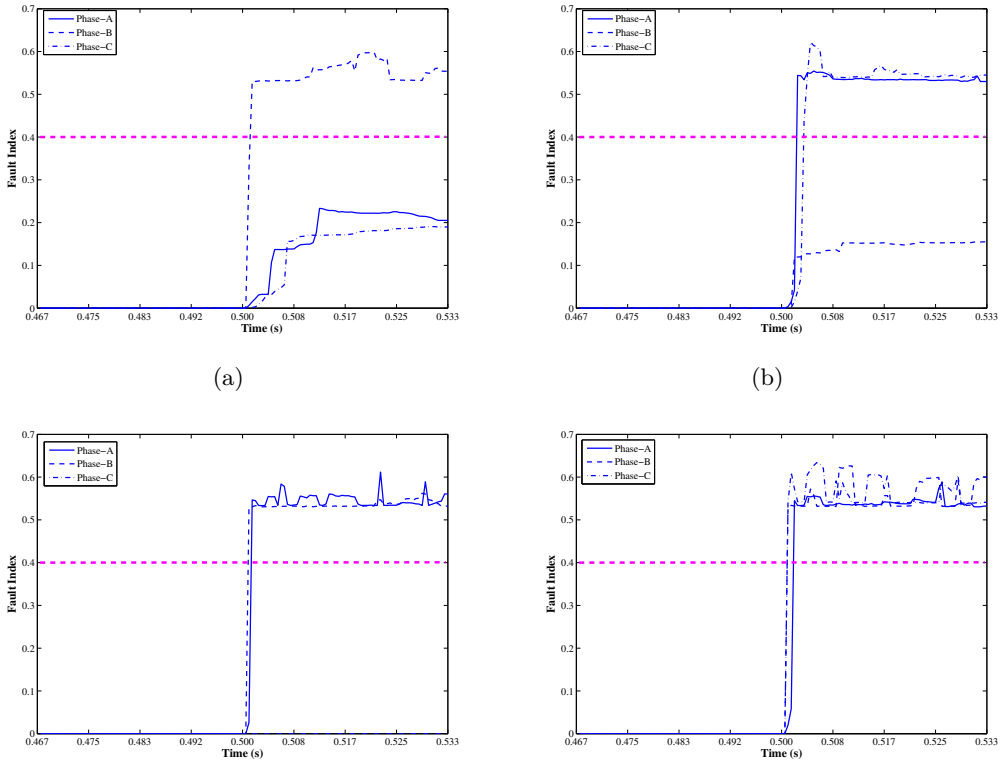

(a) (b)

(c) (d)

Figure 5.13: Variation of fault index at 611 (a) LG fault (BG) (b) LLG fault (ACG) (c) LL Fault (AB) (d) LLLG fault (ABCG).

Table 5.1: Symmetrical Dot Patterns for single phase and three phase faults at bus 611.

Fault Type	Phase-A	Phase-B	Phase-C
AG	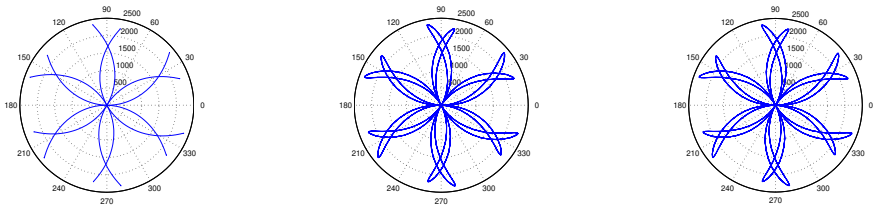		
ABG	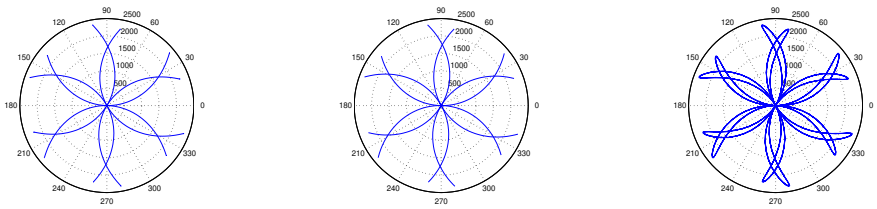		
BC	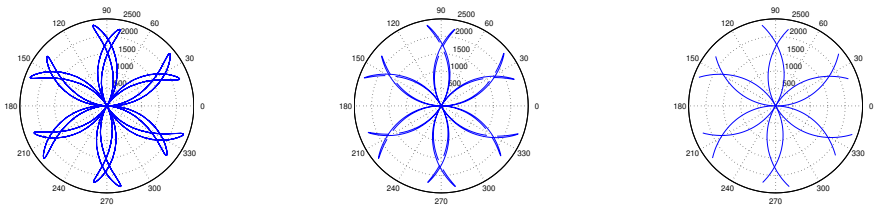		
ABCG	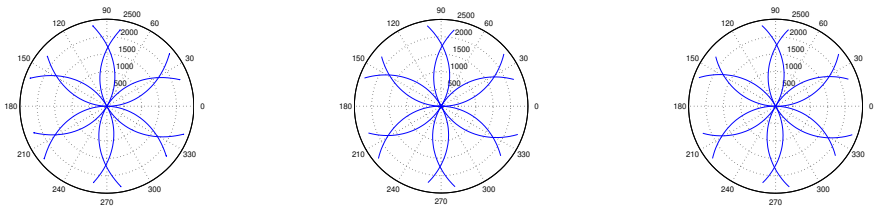		

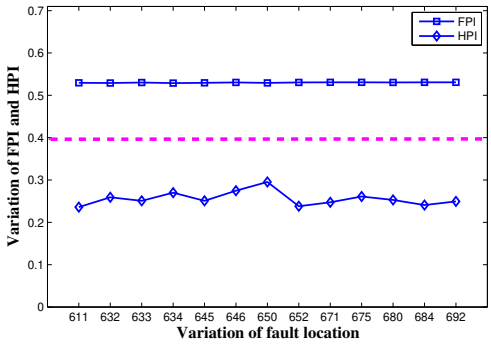

Figure 5.14: Variation of HPI and FPI with fault location.

Variation of fault resistance

Since the fault currents are affected by the variations of fault impedance, the proposed algorithm is tested for fault resistance values greater than the base impedance of 3.46 Ω for an

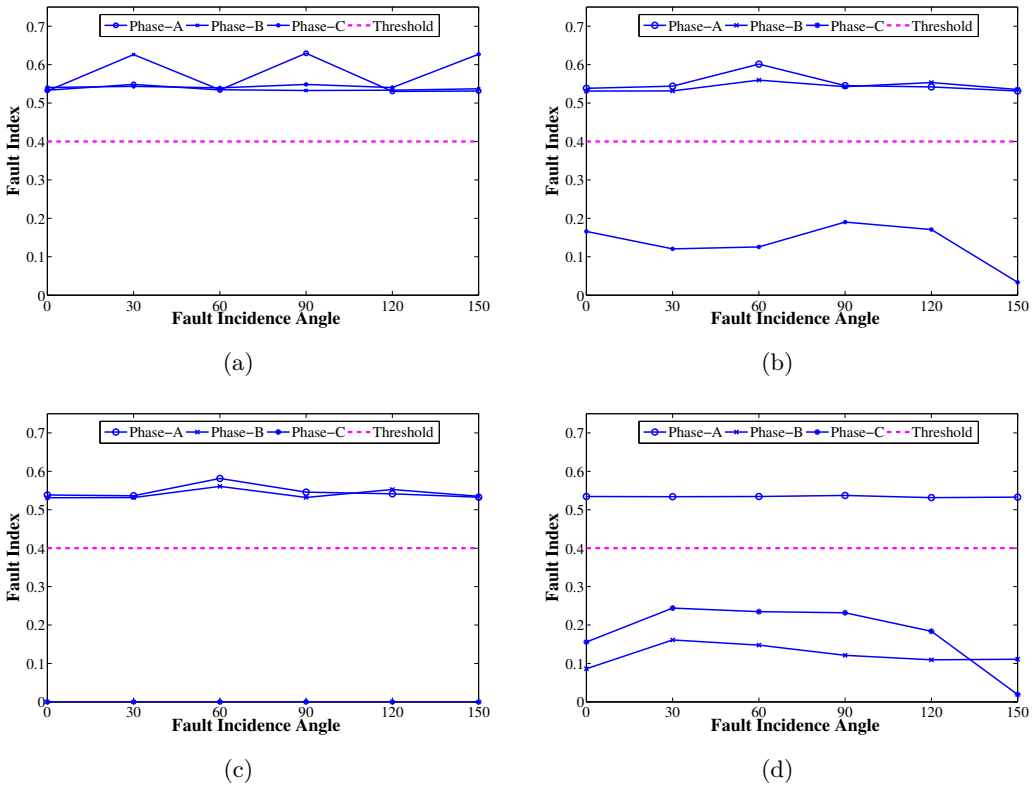

Figure 5.15: Variation of fault index with fault incidence angle at bus 632 (a) ABCG Fault (b) ABG Fault (c) AB Fault (d) AG Fault.

IEEE 13 bus system [Paz *et al.*, 2010]. The proposed algorithm is successful in detecting the faults upto 5 Ω. The detection of ABCG fault by the variation of fault resistance from 0.05 Ω to 5 Ω is shown in Fig. 5.16(a) . BG fault type is shown in Fig. 5.16(b), where the fault is only in phase-B, the other two phases A and C are below the threshold. Similar observation can be made for other faults as well.

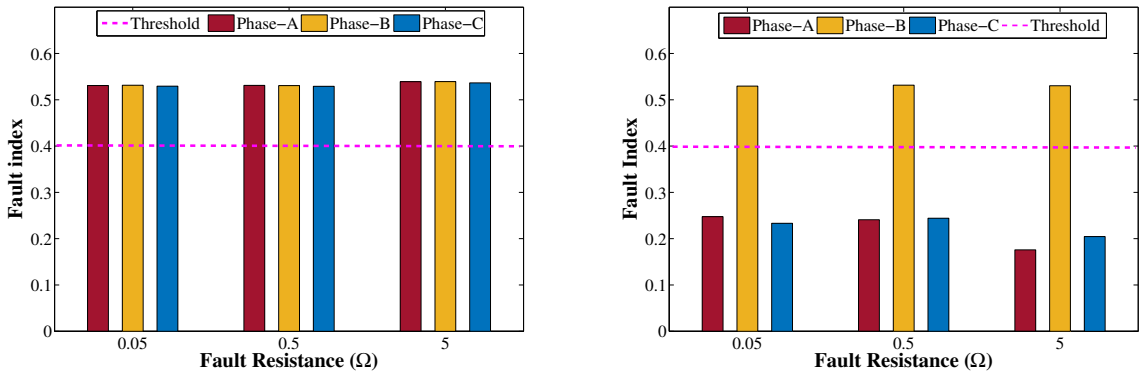

Figure 5.16: Variation of fault index with fault resistance (a) ABCG Fault (b) BG Fault.

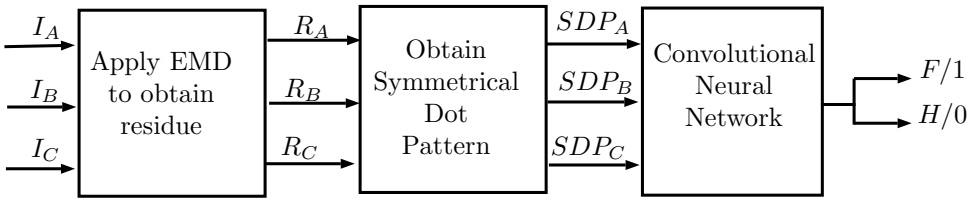

Figure 5.17: Proposed CNN based algorithm.

Table 5.2: Fault detection accuracies.

Case	Without Noise	With Noise (20 dB)	IEEE Bus system
Fault at 684 without DG	100	96.60	13 bus
Fault at 684 with DG of 800 kW	99.15	94.91	13 bus
Fault at 846 without DG	100	99.15	34 bus
Fault at 846 with DG of 400 kW	100	99.15	34 bus

5.5 PROPOSED ALGORITHM WITH DG

This section explains the application of the convolutional neural network for automatic fault detection using symmetrical dot patterns of healthy phases and faulty phases. Since it is established that a unique faulty and healthy pattern can be achieved using the last residue of the EMD process, it is essential to investigate and propose a technique to diagnose a fault automatically without feature extraction. The proposed algorithm is presented in Fig. 5.17.

The faults are considered at location 684 on an IEEE 13 bus system and 846 in an IEEE 34 bus system with solar DG and without DG. The fault currents measured at the substation are decomposed using EMD to obtain the last level residue. These residues are utilized to generate symmetrical dot patterns. The images obtained are converted to grayscale images of size 210 x 210. All the 11 types of faults are considered with six fault incidence angles at 20 dB SNR. Thus the number of images obtained are 11 x 3 x 6 = 198. Out of these, 126 images correspond to faulty phases, and 72 correspond to healthy phases. Forty images from each class are used for training the CNN, and the rest are used for testing the algorithm. The Convolution layer contains two filters of size 3x3 with a unity stride. Once these filters convolve the entire image, the resultant is a reduced matrix fed to the ReLU layer for thresholding. After the ReLU layer, the maxpooling is considered with a size of 2x2 for downsampling. After this layer, the fully connected layer multiplies the obtained matrix with weight and bias. The softmax layer converts the numbers to probabilities. Then the classification layer computes the cross-entropy loss for classification, and the most probable outcome is obtained from the output layer as a fault or healthy condition.

5.5.1 Results and Discussion

The results obtained for noise and noiseless cases are shown in the presence of DG and without DG in Table 5.2. The accuracy without noise was almost 100% and was above 94% in the presence of 20 dB noise for both the systems considered. It proves that the SDP patterns can be fed as inputs for fault detection without any feature extraction process.

5.6 PERFORMANCE COMPARISON

The proposed algorithm is compared with few existing protection schemes in Table 5.3. Only the post-fault data array considered for extracting the features is compared. As the post-fault data determines the speed of detection and classification of the protection scheme, the array considered for extracting suitable features should contain minimum fault data. It can be concluded that the SDP method is capable of detecting and classifying faults quickly within half cycle. The time elapsed for executing the algorithm for detecting the fault after SDP formation using CNN is 4.66 ms on a PC with Intel(R) Core(TM) i3-4005U CPU @ 1.70 GHz and 4 GB RAM.

Table 5.3: Comparison of Protection Schemes.

Ref	Technique	Post-fault Data	Samp Freq
[Proposed]	EMD+SDP	0.325 cycle	1.92 kHz
Samantaray *et al.* [2008]	ST+PNN	0.5 cycle	1.0 kHz
Mishra and Rout [2016a]	FDST +ELM	1 cycle	3.84 kHz
Mishra *et al.* [2016a]	WT + DM	1 cycle	6.66 kHz

5.7 HARDWARE IMPLEMENTATION OF THE PROPOSED ALGORITHMS

The algorithms developed in this thesis work are proposed for online monitoring by utilizing only the current signals. The hardware components required for the real-time implementation are a current transformer (CT), real-time Input/Output (I/O) control device like MicroLabBox from dSPACE or RTDS from Opal RT, high-speed computer, sensors, channel probes, and DSO to monitor the input and output waveforms. The current signals from the CT of the test system integrated with the utility grid, as shown in Fig. 5.18, are fed to a real-time I/O device interfaced with a PC. The real-time controller comprises of in-built A/D converter, DSP processor, and D/A converter. The moving window algorithm executed in the PC with the help of controller software acts as a relay. It monitors each new current sample and detects any fault or islanding case. The trip signal could be sent to the output port of the real-time controller to actuate the circuit breaker.

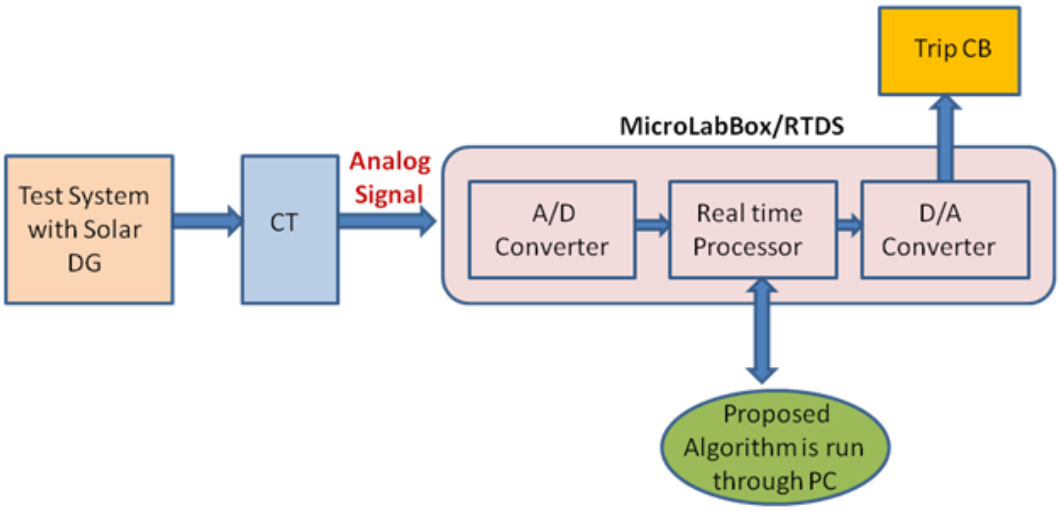

Figure 5.18: Hardware implementation of the proposed algorithms.

5.8 CONCLUSION

Unique fault pattern based method has been proposed using symmetrical dot pattern for protection of distribution network. The monotonic nature of the residues obtained from EMD is utilized to obtain SDP which are compared with the patterns obtained under normal condition. The changes in the location of the fault, fault type and the fault incidence were found to have no effect on the SDP generated and establishes the robustness of the algorithm. The fault index based on alienation technique is utilized to detect and classify the faults as fast as 0.325 cycle. The symmetrical dot patterns could pave a way for deep learning application in distribution system protection involving images by eliminating the feature extraction process.